EXCITED STATE DYNAMICS IN 1D THERMOELECTRIC MATERIALS

A Thesis
Submitted to the Graduate Faculty
of the
North Dakota State University
of Agriculture and Applied Science

By

Kevin Victor Gima

In Partial Fulfillment of the Requirements
for the Degree of
MASTER OF SCIENCE

Major Department:
Physics

April 2020

Fargo, North Dakota

North Dakota State University
Graduate School

Title

EXCITED STATE THERMODYNAMICS IN 1D THEMOELECTRIC MATERIALS

By

Kevin Victor Gima

The Supervisory Committee certifies that this ***disquisition*** complies with North Dakota State University's regulations and meets the accepted standards for the degree of

MASTER OF SCIENCE

SUPERVISORY COMMITTEE:

Dmitri Kilin
Chair

Andrei Kryjevski

Svetlana Kilina

Erik Hobbie

Approved:

4-28-2020
Date

Sylvio May
Department Chair

ABSTRACT

Here, nonadiabatic computations are used to study the thermoelectric effect and evaluate electron relaxation rates in lead telluride nanowires. $\kappa_e = \frac{1}{\tau_{\mathrm{el}}}$ is defined as the *electron relaxation rate*. It is directly connected to the thermoelectric figure of merit in a material. This work provides computational evidence in support of the proceeding hypothesis. **The hypothesis is the electron relaxation rates will comply with the following band gap law: Ke = Aexp(-αΔE)**, where Ke is the electronic relaxation rate, A and α are constants, and ΔE is the energy difference between the initial and final states. This work reports results on PbTe (lead telluride) atomistic models doped with sodium and iodine that contain approximately 300 atoms in simulation cells with periodic boundary conditions.

ACKNOWLEDGEMENTS

This thesis and the associated research could not have been completed without the aid of my advisor Dr. Dmitri Kilin. He has been a supportive and patient teacher, supportive. His forgiveness of my mistakes consistently inspired me to work harder and delve deeper into the research. His expertise and suggestions were always an email away, and he was quick to respond.

Furthermore, I would also like to thank my research group who gave strong and consistent feedback on my research. Dr. Yulun Han was always an invaluable resource to me during group meetings on research skills and scientific writing. Also, I would like to thank Fatima for her numerous grammar and punctuation corrections on this thesis. Additionally, I would like to thank Talgat Inerbaev for help in the calculations needed for this thesis. Lastly, I would like to thank the entire physics department for their consistent support and encouragement.

DEDICATION

To Victor and Ujjwala Gima, my parents who always provided me with emotional warmth. To my aunt, Shailabala Daniels and cousin, Rahul Daniels who provided me with support during my teenage years.

TABLE OF CONTENTS

LIST OF FIGURES

INTRODUCTION

Semiconductors are utilized in modern technology. Cellphones, microwaves, refrigerators, automobiles, microwaves and numerous other technologies are indispensable to modern life. Applying thermoelectric materials to them has the potential to strengthen their efficiency. Thermoelectric materials are materials that use a temperature gradient to produce a current. Their effect is measured by a material's figure of merit given by $\boldsymbol{zT} = \frac{\sigma S^2 T}{\kappa}$ where S is the Seebeck coefficient, κ thermal conductivity, σ electrical conductivity, and T temperature [(1)]. Researchers aim to maximize this parameter. Oftentimes scientists produce these materials by doping (adding impurities) various materials [(2)].

Since charge transfer is one of the primary criteria in determining a material's viability in application to the real world, it is very important in the study of semiconductors. In figure 1, before electron transfer, the left region has an excess of one electron and the right region has a hole. After some time, light energy excites one of the electrons and it fills right region's hole. This process is known as charge transfer. Charge transfer is simply the movement of electrons excited by photons to fill a hole.

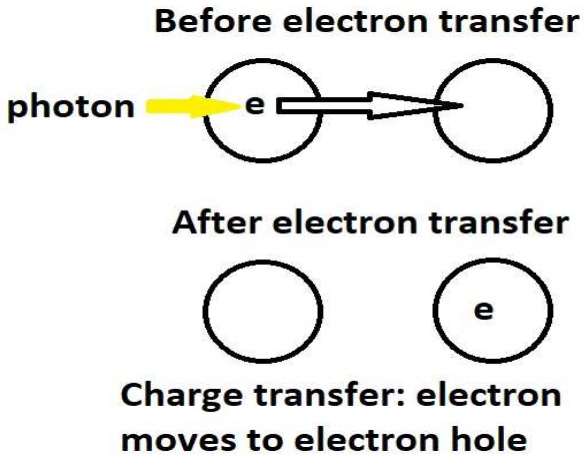

Figure 1. Illustration of charge transfer. This shows how electron travels to hole. When light excites an electron, it absorbs a photon and travels to fill the hole in atom. Charge transfer involves the movement of electrons.

In traditional semiconductors, the photovoltaic process (illustrated in figure 2) is used to excite electrons and induce a current. Light, which carries photons, shines on a material with a p-n junction. N-type materials has an excess of electron. Conversely, p-type materials have an excess of holes. When photons are introduced into a system, it gives the electron enough energy to fill the holes from the p-type material. This movement of electrons induces a current and is used to power almost all technology in our modern world.

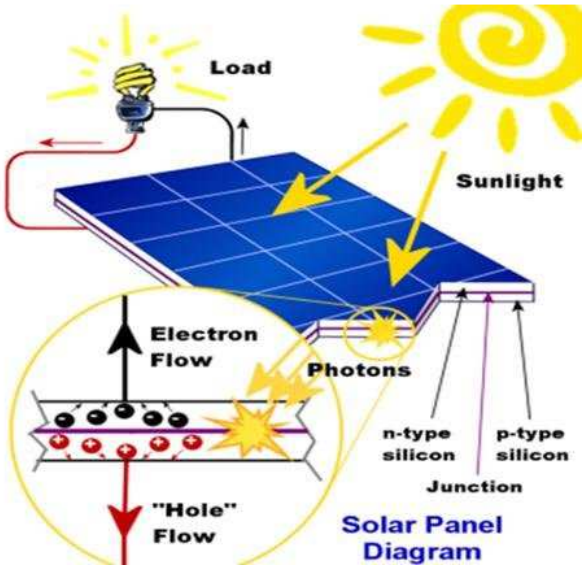

Figure 2. Illustration of the photovoltaic process [8]. Initially, light shines on the panel. After the electrons absorb the associated photon, it travels from n-type (electron) to p-type (electron). This charge transfer powers the electrical circuit illuminating the lightbulb.

In a thermoelectric material there are free electrons or holes which carry both charge and heat. To a first approximation, the electrons and holes in a thermoelectric semiconductor behave like a gas of charged particles. If a normal (uncharged) gas is placed in a box within a temperature gradient, where one side is cold and the other is hot, the gas molecules at the hot end will move faster than those at the cold end. The faster hot molecules will diffuse further than the cold molecules and so there will be a net buildup of molecules (higher density) at the cold end. The density gradient will drive the molecules to diffuse back to the hot end. In the steady state, the effect of the density gradient will exactly counteract the effect of the temperature gradient so there

is no net flow of molecules. If the molecules are charged, the buildup of charge at the cold end will also produce a repulsive electrostatic force (and therefore electric potential) to push the charges back to the hot end. This phenomenon where an electric potential (Voltage) produced by a temperature difference is known as the Seebeck effect. If the free charges are positive (the material is p-type), positive charge will build up on the cold which will have a positive potential. Similarly, negative free charges (n-type material) will produce a negative potential at the cold end. The thermoelectric effect is illustrated in figure 3.

Many believe that lead telluride is an ideal material due to scientists consistently achieving a high figure of merit. Heremans et al. (2008) achieved a figure of merit of 1.5 at 773K with a thallium-doped lead telluride [(3)]. Snyder et al. (2011) obtained a 1.4 figure of merit at 750 K with sodium-doped lead telluride [(4)], and a 1.8 figure of merit at 850K with sodium-doped $PbTe_{1-x}Se_x$ alloy [(5)]. Also, a different group of researchers produced a figure of merit of 2.2 with the material [(6)(7)].

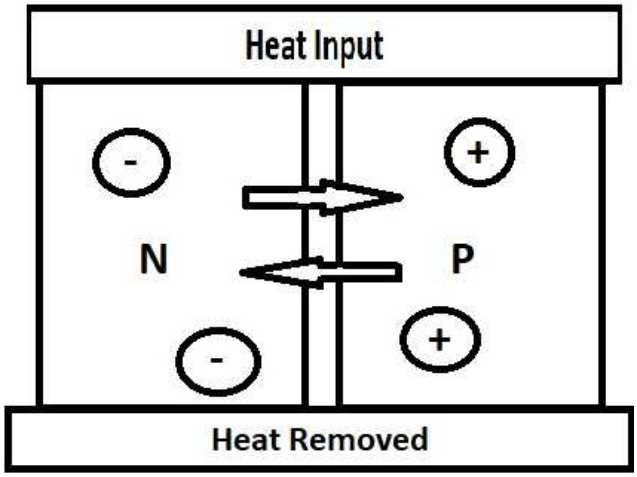

Figure 3. The thermoelectric effect. Those electrons and hole that possess greater kinetic energy on the hot side quickly migrate to the cold side. These electrons on the cold side repels the electrons remaining on the hot side and induce a voltage between the n and p-types. This voltage in turn produces a current that can be used to power appliances.

In this study, a periodic lead telluride nanowire doped with sodium and iodine (figure 4) was examined. The unit cell length is 110 angstroms and possesses a cubic structure with 288 atoms. Lead and telluride occur in a 1:1 ratio, with two iodine and sodium atoms. Lead donates its two excess electrons to telluride so it can complete its valance shell. This is illustrated in the following equation.

$$Pb^{2+} + Te^{2-} = PbTe \tag{1}$$

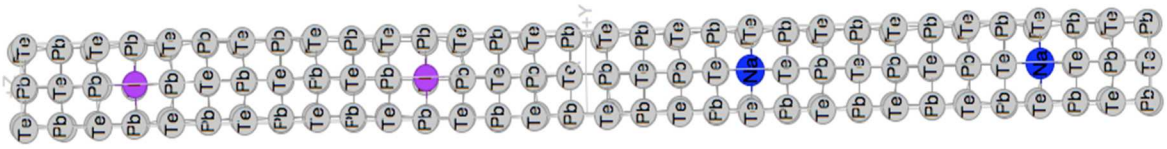

Figure 4[41]. A rectangular PbTe nanowire doped with Iodine (pink) and Sodium (blue). Sodium replaces lead atoms due to excess electrons in their valence band. Conversely, iodine replaces telluride due to excess holes in their conduction band. This study examines if this doping configuration improves charge transfer.

To understand this work one must have a minimum understanding of the charge balancing of dopants in the doping process. Doping is the process of inserting impurities into a semiconductor to modify its properties. For instance, sodium doping works as follows:

$$[Na^{(0)} \rightarrow Na^{(1+)} + 1e^-] - [Pb^{(0)} \rightarrow Pb^{(2+)} + 2e^-] = Na^{(0)} - Pb^{(0)} \rightarrow 1e^- - 2e^- = -1e \tag{2}$$

In equation (2), sodium has one extra electron in its valance band. In contrast, lead has two extra electrons. When sodium replaces lead in the doping process, one electron is displaced from the valence band.

$$[I^{(0)} \rightarrow I^{(1-)} - 1e^-] - [Te^{(0)} \rightarrow Te^{(2-)} - 2e^-] = I^{(0)} - Te^{(0)} \rightarrow -1e^- - (-2e^-) = 1e^- \tag{3}$$

In equation (3), iodine has a hole in its valance shell. As previously stated, telluride has two holes in its shell. In iodine doping, the iodine replaces the telluride. After doping, one hole is removed from the conduction band. See figure 5 below for a pictorial explanation of sodium and iodine doping.

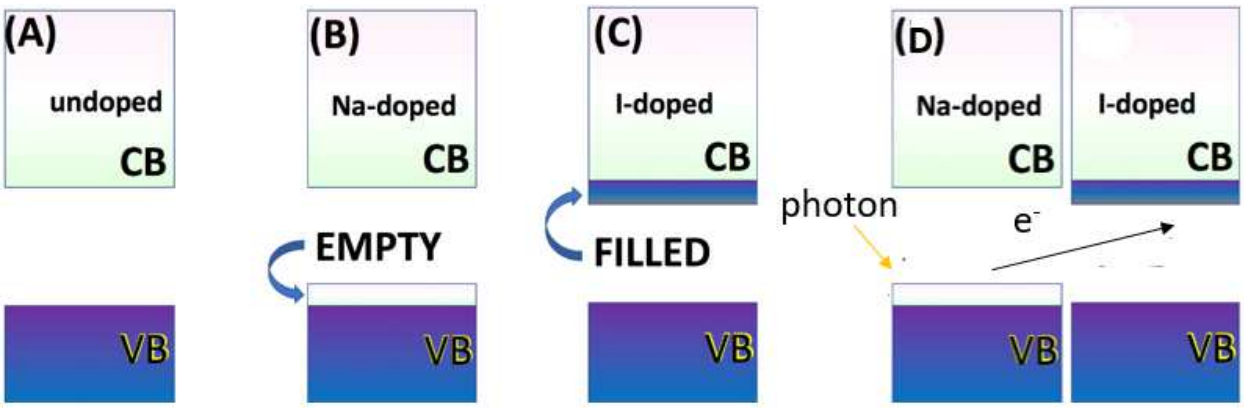

Figure 5[41]. Electronic structures of various doped and undoped nanowires. (A) In the undoped state, both valence and conduction bands are unchanged (B) In Na-doped state, one electron is taken from the valence band. (C) In the I-doped state, a hole from the conduction band is removed. In other words, this hole is filled with an electron. (D) This combines both Na and I doping. Charge transfer of an electron upon photoexcitation from sodium's valence band to sodium's conduction band is illustrated.

The basis for computational and theoretical chemistry is the time dependent molecular Schrödinger equation: $-\mathrm{i}\hbar\frac{\partial}{\partial \mathrm{t}}\psi(X,t) = \left(\widehat{H} - \hat{\mu}\cdot\vec{\mathrm{E}}(\mathrm{t})\right)\psi(X,t)$. In the case of absent perturbations, the electric field is zero $\vec{\mathrm{E}} = 0$, $\psi(X,t) = \sum_n \varphi_{\mathrm{n}}(X)\, e^{-\frac{i}{\hbar}\mathrm{E_n}t}$, and the molecular Schrödinger equation becomes independent of time: $\widehat{\mathrm{H}}\varphi_{\mathrm{n}}(\mathrm{X}) = \mathrm{E_n}\varphi_{\mathrm{n}}(\mathrm{X})$ where $\widehat{H}$ is the molecular Hamiltonian, $\psi(X,t)$ is the wave function, E_n is the eigenvalue, and $\mathrm{X} = \{\mathrm{r_i}\}\{\mathrm{R_I}\}$ includes all independent variable including positions of electrons $\{\mathrm{r_i}\}$ and ions (nuclei) $\{\mathrm{R_I}\}$.

The molecular Hamiltonian has the following form: $\widehat{H} = T_N + T_e + V_{NN} + V_{ee} + V_{Ne}$ where T_e = kinetic energy of ions, T_e = kinetic energy of electrons, V_{NN} = potential energy of ion interaction, V_{ee} = potential of electron interaction, and V_{Ne} = potential energy of the interaction between electrons and ions.

Due to computational power limits, the full form of the molecular Schrödinger equation is very difficult to solve for almost any system. To compensate, separation of variables is implemented to transform the equation from one multidimensional equation to several one-

dimensional equations. While this is very simple for the $T_N, T_e,\ V_{NN}, and\ V_{ee}$ terms, the V_{Ne} term is difficult due to the incorporation of both electron and ionic variables.

Computational and theoretical chemists, physicists, and other researchers use the Born-Oppenheimer approximation to deal with the V_{Ne} term. Since the ions' mass are much greater than the electrons' mass, Born and Oppenheimer utilize a two-part approximation. First, the nuclei's equilibrium positions are used to solve the electronic wavefunction. Second, the ground state electronic energy is applied as potentials in the ionic portion of the wavefunction. In this manner, the molecular Schrödinger equation is solved by separating the equation into an electronic part and an ionic part, as follows: Electronic: $\left(\hat{T}_e\ +\ \hat{V}_{ee}\ +\ \hat{V}_{Ne}\right)\phi_a = E_a(R)\phi_a$ where ϕ_a is the wave function and $E_a(R)$ is the Eigenvalue based on position R. Ionic: $i\hbar\frac{d}{dt}\chi_b(R,t) = \left(\hat{T}_N^{pure} + \hat{V}_{NN} + E_b(R)\right)\chi_b(R,t)$ where: $i\hbar\frac{d}{dt}$ is time derivative, $\chi_b(R,t)$ is the ionic wavefunction, and $E_b(R)$ is energy from the electronic equation above.

These equations are then solved by a computer by using one of the established theories. Examples include Hartree-Fock, CI Coupled Cluster, or density functional theory (DFT) method in order to calculate electronic properties.

All computational methods use numerical results to find the lowest total energy. In density functional theory, the electronic density is used in lieu of the wavefunction. Thus, the total energy is a functional of it. Computational chemistry researchers regularly offer new formulas for such functionals targeting better precision. Density functional theory represents molecular orbitals with basis sets. Understanding the difference between density functional theory and its implementations enables practical implementations the theory in calculating density of states, optical absorption spectra, partial density files, and other useful properties. Although DFT is accurate enough for the

ground state, researchers are finding that more complicated and computationally extensive methods are needed for excited state dynamics and analysis.

This complex modeling helps researchers obtain more accurate predictions of excitation states' properties. The two types of excitations are optical and thermal. Photons induce optical excitations that changes the electronic state. Thermal excitations by phonons change the ions' position. Thermalized molecular dynamics models the motion of atoms along with their change in energy with time. The motion of the atoms is defined by Newton's equations and the potential energy and force are incorporated using force fields or recomputed at each step via electronic structure methods and using Hellman-Feynman Theorem.

An important challenge is assessing changes in electronic degrees of freedom induced by interaction with nuclear degree of freedom. The explicit monitoring of both eelectronic and nuclear degrees of freedom is often forbidden by high computational cost. There is a popular way to address this challenge by using so-called "open quantum system" approach, where primary system of interest, experience influence of environment in the thermal equilibrium. Often, primary system is represented by electronic degrees of freedom and environment in thermal equilibrium is represented by nuclear degreed of freedom. This approach extends the concept of density operator from static domain to dynamic domain.

Density operator characterizes quantum state of the system and is more general concept that wavefunction. In case density operator is available, one can use it for calculating expectation value for any operator representing an observable, by the trace operation: $\langle A \rangle = Tr(\hat{\rho}_{tot}\, \hat{A})$. The density operator of the complete system can be converted into *reduced density operator* of the electronic degrees of freedom, by performing averaging procedure over all nuclear degrees of freedom, which are assumed to reside in thermal equilibrium. Most interesting and useful is the

application of the density operator concept to situations when primary system is prepared in the nonequilibrium states and performs time evolution towards the equilibrium. There are several practical implementations for describing such dynamics. At thermal equilibrium, the absorbed energy can potentially cause excitations best studied and analyzed with the Redfield equation [9][10]. The Born-Oppenheimer approximation is of limited applicability to important processes such as charge transfer and relaxation in one-dimensional lead telluride nanowires, which is due to energy flow between the electronic part and nuclear part [11][12]. The electronic relaxation process based on surface hopping between potential energy surfaces was successfully completed by several groups [13]. Various methods ranging from density functional theory [14-16] to high-precision non-adiabatic excited state molecular dynamics [17-20] have been utilized to model this process in other structures. The feasibility of molecular dynamics trajectory for computing the electron-to-lattice coupling in semiconductors seems very efficient [21][22]. The integration of TDDFT and molecular dynamics methods was recently proven to be an efficient approach [23][24].

According to Egorova et al [25]., multilevel Redfield theory is a useful approach for electronic relaxation. This theory is efficient in the limits of lengthy dynamics, low couplings, and multiple electronic states [9, 25-32]. This theory is further supported by a compromise between precision and practical efficiency. The balance between the following benefits, shortcomings, and features of Redfield theory is considered while selecting a method for this work: (i) Redfield theory is a specific application of the density matrix equation of motion and, therefore it predicts the electronic properties of more phenomena as opposed to the wavefunction, surface hopping, or Pauli Master equation approaches: (ii) Redfield theory is easily used in tandem with *ab initio* computation. It is clear which parameters must be computed and used, with an efficient algorithm for computation. (iii) Redfield theory might not be the most precise, for example a method of non-

equilibrium Green's function is more general and potentially precise, but much less practical [33]. There is an attempt to combine Redfield theory with electrons-to-lattice coupling to achieve on-the-fly electron and hole relaxation [34][35]. Optimum results are expected in the following conditions: ions are considered as point charges, lattice vibrations instantaneously equilibrate with a thermostat, coupling autocorrelation function decays abruptly leading to Markov approximation, vibrational reorganization is neglected, and excited state potential energy surfaces are assumed to have the same shape as the ground state.

METHODS

The electronic structure is determined by using density functional theory (DFT)[36] implemented in the VASP software[37]. Kohn-Sham equations are employed to self-consistent DFT functions to get better approximation. The main equation is a fictitious one-electron Kohn-Sham[38] equation

$$\left(-\hbar^2/_{2m}\nabla^2 + v\left[\{\vec{R}_I\}, \vec{r}, \rho(\vec{r})\right]\right)\varphi_i^{KS}\left(\{\vec{R}_I\}, \vec{r}\right) = \varepsilon_i\left(\{\vec{R}_I\}\right)\varphi_i^{KS}\left(\{\vec{R}_I\}, \vec{r}\right) \quad (4)$$

where first term corresponds to kinetic energy T and uses symbol of gradient $\nabla = \left(\frac{\partial}{\partial x}, \frac{\partial}{\partial y}, \frac{\partial}{\partial z}\right)$. In the equation (3) we find set of one-electron orbital's $\varphi_i^{KS}\left(\{\vec{R}_I\}, \vec{r}\right)$ and their energies ε_i. The orbitals are combined with orbital occupation function f_i for constructing the total density of electrons:

$$\rho(\vec{r}) = \sum_i f_i \varphi_i^{KS^*}(\vec{r})\varphi_i^{KS}(\vec{r}) \quad (5)$$

Note that the density is composed out of pairs of orbitals with coinciding indices. Total density determines the potential:

$$v[\vec{r}, \rho] = \delta/\delta\rho(E^{tot}[\rho] - T[\rho]) \quad (6)$$

which is defined as functional derivative of the total energy in respect to variation of the total density and includes interactions of electrons with ions, and three electron interactions: Coulomb, correlation, and exchange. Rectangular brackets symbolize functional. Equations (4)-(6) are solved in the iterative, self-consistent manner by using VASP software according to Perdew–Burke–Ernzerhof procedure (PBE-functional)[39][40]-although the use of other functionals is also possible. The electron density of states (DOS) describes the number of states per interval of energy. One uses DOS to characterize electronic structures of the studied models. DOS is defined as

$$n(\varepsilon) = \sum_i \delta(\varepsilon - \varepsilon_i) \quad (7a)$$

where the Dirac delta function was approximated with a finite width Gaussian function.

One of the parameters obtained from the DFT calculation is the *oscillator strength* representing probability that a model, which absorbs a photon will undergo an electronic transition. Thus, the oscillator strength is related to the rate of absorption and is defined as:

$$f_{ij} = \frac{4\pi m_e \omega_{ij}}{3he^2} \left|\vec{D}_{ij}\right|^2 \quad (7b)$$

where $\omega_{ij} = \frac{\varepsilon_i - \varepsilon_j}{\hbar}$ is the angular frequency required to excite an electron from state *i* to state *j*. $\vec{D}_{ij} = e \int d\vec{r}\ \varphi_i^*(\vec{r}) \cdot \vec{r} \cdot \varphi_j(\vec{r})$ is the transition dipole moment for transition from state *i* to state *j,* and m_e, *h*, and *e* are fundamental constants.

The spectral density of absorption was calculated analogously to the DOS using:

$$\alpha\ (\omega) = \sum_{i \le HO} \sum_{j \ge LU} f_{ij}\ \delta(\hbar\omega - \hbar\omega_{ij}) \quad (8a)$$

Here, two sums run over *pairs of orbitals*. Each delta function is weighted by the oscillator strength corresponding to the transition so that the more probable transitions are given a greater weight in the total absorption spectrum. Delta function is approximated by the finite width function with width parameter corresponding to spectral line broadening due to the Heisenberg uncertainty principle and thermal fluctuations. The orbitals computed by eq. 4 are visualized and interpreted in form of 3D isosurfaces of partial charge density, for selected orbital $\left|\varphi_i^{KS}(\vec{r})\right|^2$ or by 1D distributions

$$\rho_i(z) = \iint dxdy \left|\varphi_i^{KS}(x, y, z)\right|^2 \quad (8b)$$

The main goal of this work is to explore nonequilibrium dynamics of electronic state of the models of interest. There are two important factors that determine nonequilibrium dynamics: initial excitation and nonradiative relaxation originating from interaction between electronic and nuclear degrees of freedom. Generally, one can assess interaction of electronic and nuclear degrees of freedom based on response of electronic system to elongation of nuclear degrees of freedom along

normal mode coordinates. Such approach is often used for solids at low temperatures when nuclear motion is described as harmonic oscillations near equilibrium. However, at elevated temperatures, in the non-harmonic regime, one often used so called "on-the-fly" evaluation, which is computed along nuclear trajectories. This approach was developed by such researchers as John Tully, Sharon Hammes-Shiffer, Oleg Prezhdo, Sergei Tretiak, Hans Lishka, and others. In order to implement this approach, one first needs to review basics of the computation of first principles molecular dynamics trajectory which is accomplished in two stages: so called HEATING and actual MOLECULAR DYNAMICS. After initial calculations using DFT and VASP software, the system is then heated to a specific temperature which increases its kinetic energy.

$$\sum_{I=1}^{N} \frac{M_I \left(\frac{d\vec{R}_I}{dt}|_{t=0}\right)^2}{2} = \sum_{I=1}^{N} \frac{\left(\vec{P}_I\right)^2}{2M_I} = \frac{3}{2} N k_B T \tag{9}$$

HEATING. The heating algorithm them reheats or cools the system depending on if the average atoms' momenta is higher or lower for the specific temperature. The system is then allowed to move for an infinitesimal amount of time, to redistribute between kinetic and potential energy domains. This procedure is repeated several times until kinetic energy stabilizes near requested value. The heating step provides initial conditions for the next step, for the molecular dynamics. The positions $\{\vec{R}_I(t)\}$ and momenta $\{\vec{P}_I(t)\}$ at the last step of the heating stage are used as input parameters, as initial conditions for the molecular dynamics stage.

MOLECULAR DYNAMICS. After the heating step, the molecular dynamics step begins.

$$\frac{d^2\vec{R}_I(t)}{dt^2} = \frac{1}{M_I}\vec{F}_I(t) \tag{10}$$

Here, the trajectory of each ion $\vec{R}_I(t)$ is obtained by integrating Newton's equation motion with initial conditions originating from the heating stage. Note that, in the *ab initio* molecular dynamics,

the Force $\vec{F}_I(t)$ is recomputed at each time step based on electronic structure data, as an observable, using Hellman Feynman theorem.

After obtaining position and expectation values using first principles molecular dynamics, nonadiabatic couplings were utilized to determine how they changed with time. The nonadiabatic coupling is the tool to assess the interaction between electronic and nuclear degrees of freedom. The nonadiabatic coupling is the measure of maintaining or violating of the orthogonality between two orbitals:

$$V_{ij}(t) = -i\hbar < \psi_i^{KS}\{\vec{r}, \vec{R}_I(\mathrm{t})\}|\frac{d}{dt}|\psi_j^{KS}\{\vec{r}, \vec{R}_I(\mathrm{t})\} >$$

$$= \frac{-i\hbar}{2\Delta t}\iiint d\vec{r}\left(\psi_i^{KS*}\{\vec{r}, \vec{R}_I(\mathrm{t}+\Delta t)\}\psi_j^{KS}\{\vec{r}, \vec{R}_I(\mathrm{t})\} + \psi_i^{KS*}\{\vec{r}, \vec{R}_I(\mathrm{t})\}\psi_j^{KS}\{\vec{r}, \vec{R}_I(\mathrm{t}+\Delta t)\}\right) \quad (11)$$

In the equation (11) we find how the orthogonality of two orbitals, $\varphi_i^{KS}\left(\{\vec{R}_I\}, \vec{r}\right)$ and $\varphi_j^{KS}\left(\{\vec{R}_I\}, \vec{r}\right)$ is kept or violated if the orbitals are evaluated at nearby steps of the nuclear trajectory, offset by timestep $2\Delta t$. One computes the coupling $V_{ij}(t)$ for all available pair of the orbitals. The value of such coupling for a provided pair of orbitals does experience oscillations, and needs two things: (A) to be averaged and (B) to be transferred from time domain to frequency domain, as described in what follows:

(A) The averaging procedure is performed in terms of the autocorrelation function computed for two pairs of orbitals $\mathrm{V}_{\mathrm{ij}}^{\mathrm{NA}}(\mathrm{t}+\tau)$ and $\mathrm{V}_{\mathrm{kl}}^{\mathrm{NA}}(\mathrm{t})$ evaluated at different times.

$$\mathrm{M}_{\mathrm{ijkl}}(\tau) = \frac{1}{\mathrm{T}}\int_0^{\mathrm{T}} \mathrm{V}_{\mathrm{ij}}^{\mathrm{NA}}(\mathrm{t}+\tau)\mathrm{V}_{\mathrm{kl}}^{\mathrm{NA}}(\mathrm{t})\mathrm{dt} \quad (12a)$$

This autocorrelation function uses an average over the time interval *T*, which is the duration of the whole trajectory. In addition, thee autocorrelation function is related to the transition rate between orbitals. Also, note that most important elements of the autocorrelation are those with coinciding

pairs of indices M_{ijij}, which deal with population relaxation. Other values do correspond to decoherence.

(B) The Fourier transform of $M_{ijkl}(t)$ is often referred to and Redfield tensor and is denoted as R_{ijkl}.

$$R_{ijkl} = \Gamma^{+}_{ljik} + \Gamma^{-}_{ljik} - \delta_{lj}\sum_m \Gamma^{+}_{immk} - \delta_{ik}\sum_m \Gamma^{-}_{lmmj}, \tag{12b}$$

$$\Gamma^{+}_{ijkl} = \int d\tau\, M_{ijkl}(\tau)\exp(-i\omega_{kl}\tau), \tag{12c}$$

$$\Gamma^{-}_{ijkl} = \int d\tau\, M_{ijkl}(\tau)\exp(-i\omega_{ij}\tau), \tag{12d}$$

The details on the computation of this tensor are available in the original paper by A.G. Redfield and a range of papers on nonequilibrium dynamics. The elements of the Redfield tensor have an analogy to Fermi's golden rule. A transition from instantaneous nonadiabatic coupling to the rates averaged over trajectory corresponds to Markoff approximation and allows to formulate differential equation of motion for density operator without memory kernel.

After calculating this transition rates, density matrix dynamics is used to find how the density operator changes with time.

$$\frac{d}{dt}\hat{\rho}(t) = -\frac{i}{\hbar}[H, \hat{\rho}(t)] + \hat{\mathrm{R}}\hat{\rho}(t) \tag{13a}$$

After substituting in in the definition of density $\rho(\vec{r}) = \sum_{ij}\rho_{ij}\varphi_j^{KS^*}(\vec{r})\varphi_i^{KS}(\vec{r})$ into eq. 13 one obtains the equation in terms of density matrix and matrix elements.

$$\frac{d}{dt}\rho_{ij}(t) = -\frac{i}{\hbar}\sum_k (H_{ik}\rho_{kj} - \rho_{ik}H_{kj}) + \sum_{kl} \mathrm{R}_{ijkl}\,\rho_{kl}(t) \tag{13b}$$

Note that the density considered here is time dependent. It contrasts the ground state density in the original density functional theory, which is time independent. After the density matrix

dynamics trajectory $\rho_{ij}(t)$ is calculated, one can move to the task of computing observables. Note that the diagonal elements of density matrix ρ_{ii} correspond to population of orbital *i*.

Observables

The overall picture of charge density evolution in time can be analyzed in form of mapping solution for density matrix into distribution as function of energy

$$n(\varepsilon, t) = \sum_i (\rho_{ii}(t) - \rho_{ii}(\infty))\, \delta(\varepsilon - \varepsilon_i) \tag{14}$$

The expectation value of electron and hole energy is calculated using:

$$< E_{e/h} > (\mathrm{t}) \; = \; \sum_{i \geq LU} \rho_{\mathrm{ii}}\,(\mathrm{t}) \varepsilon_{\mathrm{i}}(\mathrm{t}) \tag{15a}$$

$$< E_h > (\mathrm{t}) \; = \; \sum_{i \leq HO} \rho_{\mathrm{ii}}\,(\mathrm{t}) \varepsilon_{\mathrm{i}}(\mathrm{t}) \tag{15b}$$

Note that $\sum_i \rho_{\mathrm{ii}} = 1$. Finally, the rate of relaxation is calculated using the following:

$$k_{e/h} = \frac{d < E_{e/h} >}{dt} \tag{16}$$

$$k_{e/h} = \left\{\tau^{e/h}\right\}^{-1} = \left\{\int_0^{\infty} \langle E_{e/h} \rangle (t) dt\right\}^{-1} \tag{17}$$

The main goal of this study is to determine if the relaxation rates follow the band gap law below:

$$k_{e/h} = A e^{-\alpha \Delta \mathrm{E}} \tag{18}$$

Also, it is important to note that charge density evolution in time can be analyzed in form of mapping solution for density matrix into distribution as function of space

$$n(z, t) = \sum_i (\rho_{ii}(t) - \rho_{ii}(\infty))\, \rho_i(z) \tag{19}$$

RESULTS

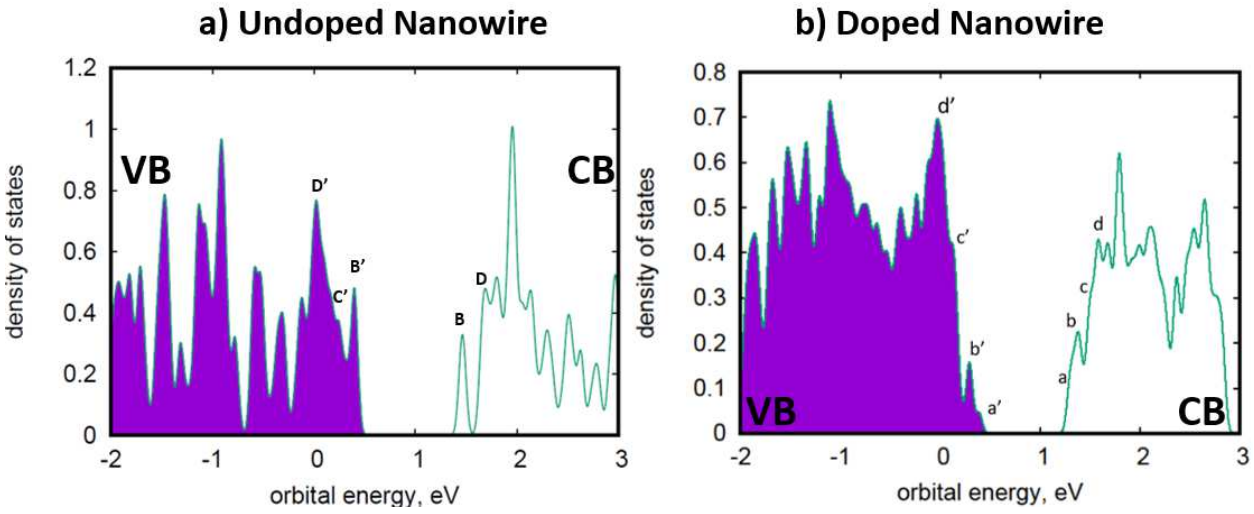

Figure 6. Density of states. Note that the filled area for doped nanowire is greater than undoped, indicating a greater number of states. Furthermore, the doping process added extra states a and c in the conduction band and a' in the valence band. a and a' are congruent with the extra states added to both band in figure 5d.

Figure 6 shows density of states for the undoped and co-doped PbTe NW, computed according to Eq. 7(a). Figure 6(a) shows an undoped lead telluride rectangular nanowire. The bandgap here is approximately 1 eV. In the conduction band, the orbitals with energies ranging from 1.5 to 2 eV will have the greatest number of states. This is supported by figure 6(b) for the co-doped nanowire. In the valence band above (from -2 to 0) we see that at energies 0 and -1 there is the greatest number of states available. Note the purple color indicates that these states are occupied by electrons. Note that a greater number of states are accessed for the doped model. Furthermore, the bandgap here has slightly decreased to 0.9 eV. These two changes indicate a drastic increase in the co-doped nanowire's ability to facilitate charge transfer.

Unoccupied conduction band peaks B,D in 6(a) correspond to unoccupied conduction band peaks b, d in 6(b). Peaks a, c in co-doped are unique and do not have counterparts as they are contributed by iodine. Occupied peaks B',C', D' in valence band of 6(a) correspond to occupied peaks b',c',d' in valence band of 6(b). The occupied peak a' in co-doped VB does not have analogs

as it is contributed by sodium. So, it can be concluded from analysis of DOS, that the frontier orbitals of the co-doped model are contributed by dopants and the lowest excitation is expected to have the charge transfer character.

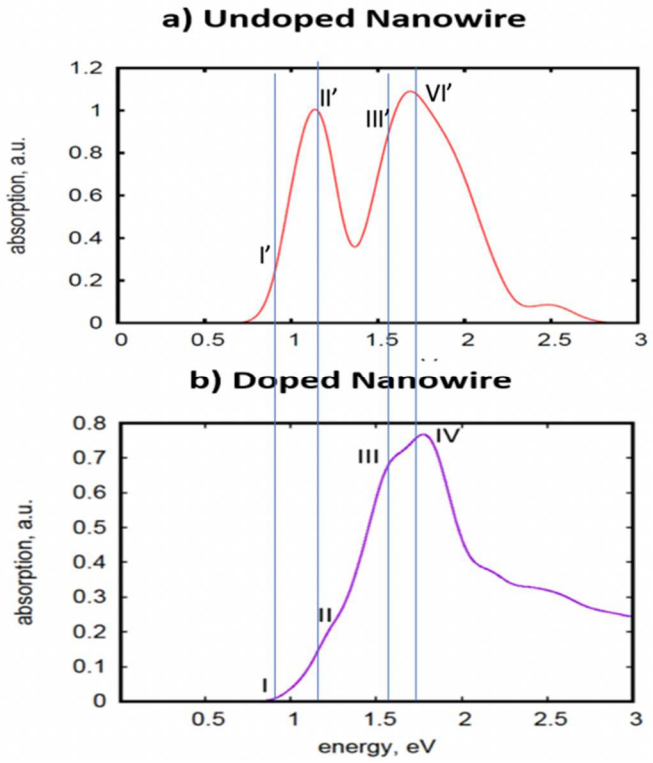

Figure 7. Absorption spectra of (a) undoped and (b) doped nanowires. In (a), the lowest transition is bright due to non-overlap between B and B' in figure 6(a). In contrast, lowest transition in (b) is dark due to charge transfer excitation.

Figure 7 presents absorption spectra of the undoped and co-doped models, computed by equation 8. Overall intensity of absorption is higher for undoped than for the co-doped model. In figure 7(a), the transition from B' to B is expected to be bright due to their delocalization over telluride and lead ions, respectively. Thus, these states will have significant overlap and therefore increased value of oscillator strength.

Additionally, in figure 7(b), the absorption spectra of the doped nanowire are shown in comparison with the undoped nanowire. Note that the lowest transition (I) from a' to a in figure 6(b) is dark due to charge transfer excitation. This is congruent with the expected results since the

electron is experiencing a transition between orbitals with different spatial localization, and negligible overlap, that disables the intensity of optical transition. Note that a' and 'are localized near the sodium and iodine dopants, respectively. In short, (a) & (b) differ due to new doped states a and c.

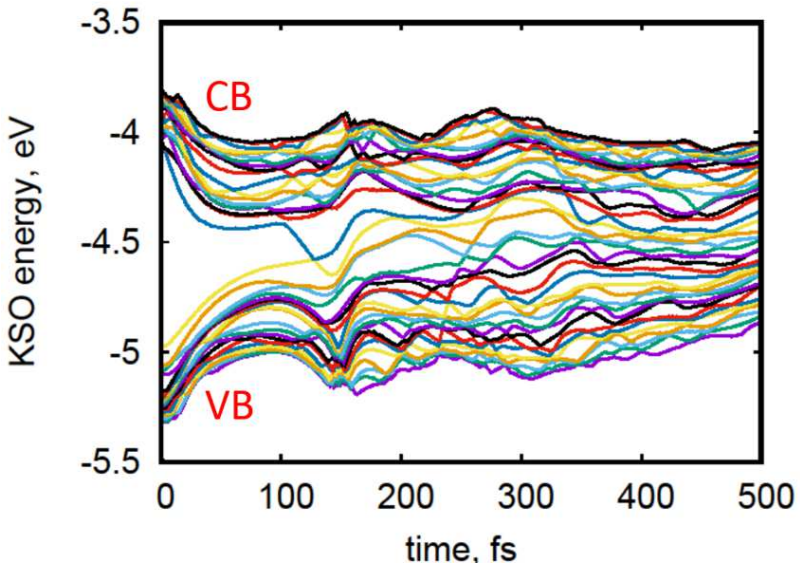

Figure 8. Kohn-Sham orbital energies as a function of time at 1000K. This shows that the bandgap is inversely proportional to time. In other words, it decreases with time. Note that the system was heated for 50 fs at 1000K and was subsequently utilized for molecular dynamics simulations for 1000 fs.

Figure 8 represents an example of Kohn-Sham orbital energies fluctuating along molecular dynamics trajectory. It is very interesting to discuss how the bandgap changes with time. Since $R_I = R_I(t)$ and $\varepsilon_I = \varepsilon_I(R)$, this implies that $\varepsilon_I = \varepsilon_I(R_I(t))$ where R_I and ε_I stand for the position of the nucleus and energy of the orbital respectively. Positions are computed by Equation (10) and energies of orbitals are computed by equation (4). Note that upper case latin indices label nuclei and lower case latin indices label orbitals. In other words, the energies depend on the nucleus' position which in turn depend on time. Initially, in figure 5, the bandgap is approximately 1 eV at t=0 femtoseconds. Figure 8 was taken when the system was heated to 1000K. Initial 150 fs in Figure 8 show the interval of the dynamics when the model did not reach thermal equilibrium.

During this time interval there is an interesting observation of the gap dynamically changing in time. As time progresses, the bandgap decreases until it eventually becomes zero. After t>150fs, the model is in the equilibrium and can be used for productive generation of nonadiabatic couplings.

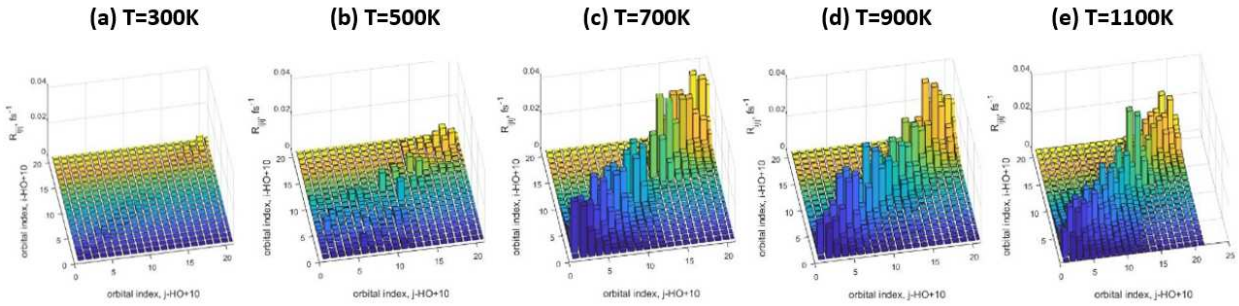

Figure 9. Redfield tensors at various temperatures. This figure shows the transition rates orbital i-HO+10 and orbital j-HO+10. The rates undergo a substantial increase at 700 K. Subsequently, the rates appear to equalize along the main diagonal.

Figure 9 shows elements of Redfield tensors computed by Equations 12(b)-12(d). Figure 9 shows that the rates of transitions between orbitals increase if we put system on a thermostat with larger temperature. One interpretation of this is as follows. At higher temperatures, the amplitude of fluctuations increases, and orbitals gaps/sub gaps temporarily close. This could be one of the underlying mechanisms increases the transition rate. Another underlying mechanism is that larger amplitude of nuclear motion gives larger violation of the orthogonality. Note that temperature fluctuations as shown in previous figure contribute to enhancement of relaxation rates.

At initial temperatures, the transition rates near the bandgap are close to zero. Note that the graphs above show a positive correlation between the temperature and transition rate. This is expected. As temperature increases electrons will have more energy to jump between orbitals. Note that this is also due to a change in time. Furthermore, as temperature increases the gap between the conduction and valence band decreases. Another feature of interest is that at lower temperatures most orbitals near HOMO and LUMO have negligible transition rates. However, as

temperature increases transition rates are more evenly distributed among orbitals. States in middle contribute to PbTe→PbTe transitions, states in top right are PbTe→I transitions, and states in top left are PbTe→Na transitions

Additionally, the orbitals furthest from HOMO and LUMO have very high transition rates as shown in figure 9. This is consistent with figure 5. At the start of the time step the bandgap is around 1 eV. However, as time goes on and temperature increases, the bandgap decreases and the transition rates for orbitals adjacent to HOMO & LUMO increase. There are two causes: the temperature increase and nonequilibrium dynamics. The second one is congruent with the differences in panels a and e. At 1100K (panel e), the transition rates among orbitals are somewhat more in congruent than in panel a. However, at later temperatures these transition rates increase.

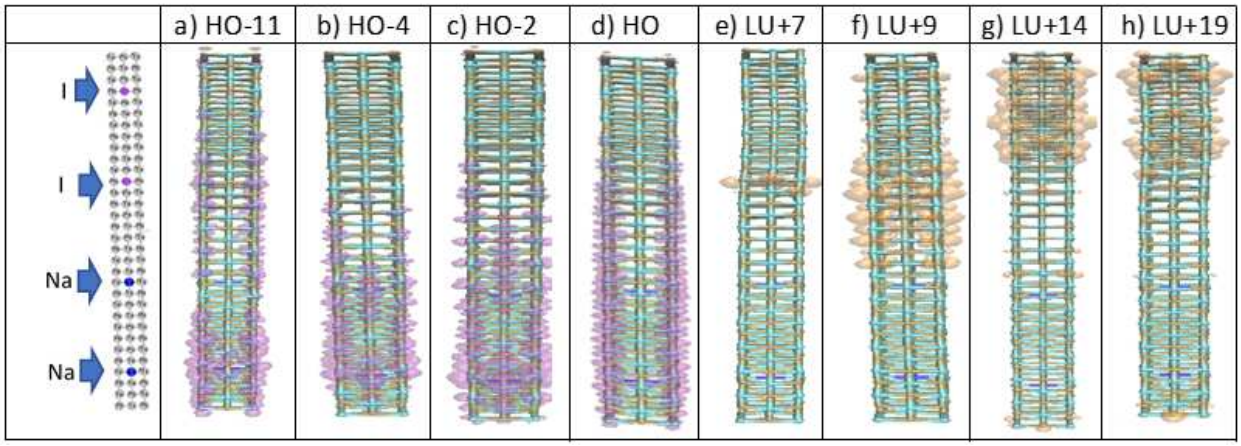

Figure 10. Orbital localization. This figure shows all orbitals that were considered in this study. Note that all HO orbitals are localized near the sodium dopants, Conversely, all LU orbitals are localized around the iodine dopants.

Figure 10 shows all orbitals that were considered in the study. The most important trend to note here is orbital localization. In other words, all the occupied orbitals are found near the sodium dopants, and the unoccupied orbitals are near the iodine dopants. This is consistent with the chemical structure of both iodine and sodium. The best example for this is in figure 10(d) which

illustrates the HOMO. In this case, it is clearly shown that all occupied orbitals are localized around the sodium orbitals. Likewise, all the unoccupied orbitals are near the iodine dopants.

Figure 11 illustrates 1D distributions of Kohn-sham orbitals computed by Equation 8(b). Figure 11 further supports figure 10. This shows that the conduction and valence bands are centered around the I and Na dopants respectively, in agreement with the preceding figure. Also, the probability density for the unoccupied orbitals are higher. This is expected since the electron is traveling to fill the hole in iodine.

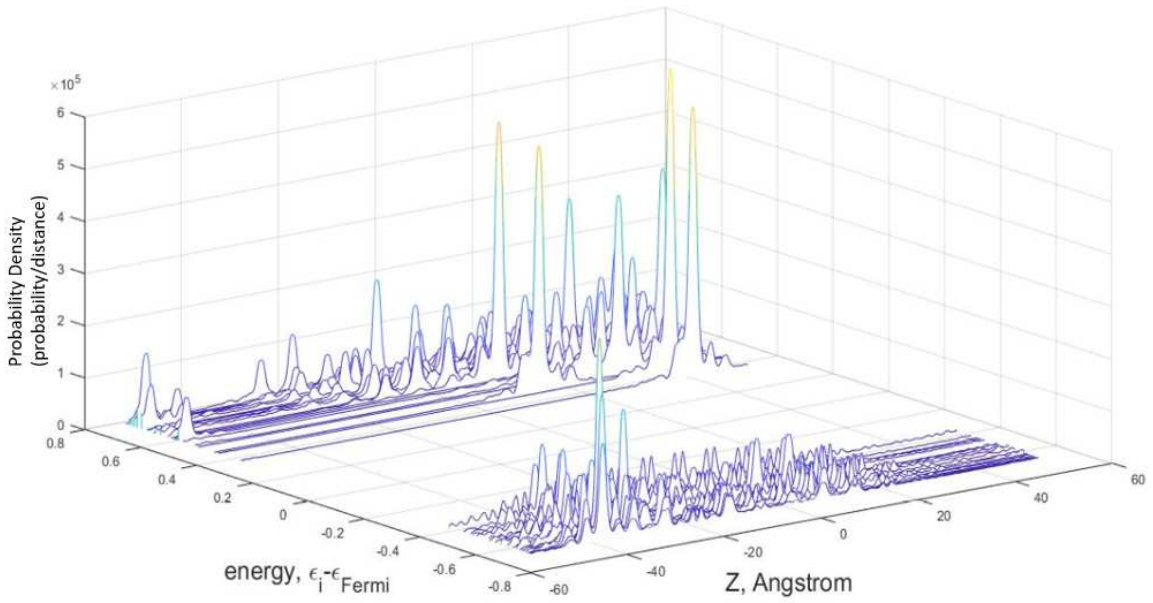

Figure 11. Probability density as a function of atomic distance and orbital energy. Congruent with figure 10, the conduction and valence bands are localized around the sodium and iodine dopants. Note that probability appears highest at the conduction band.

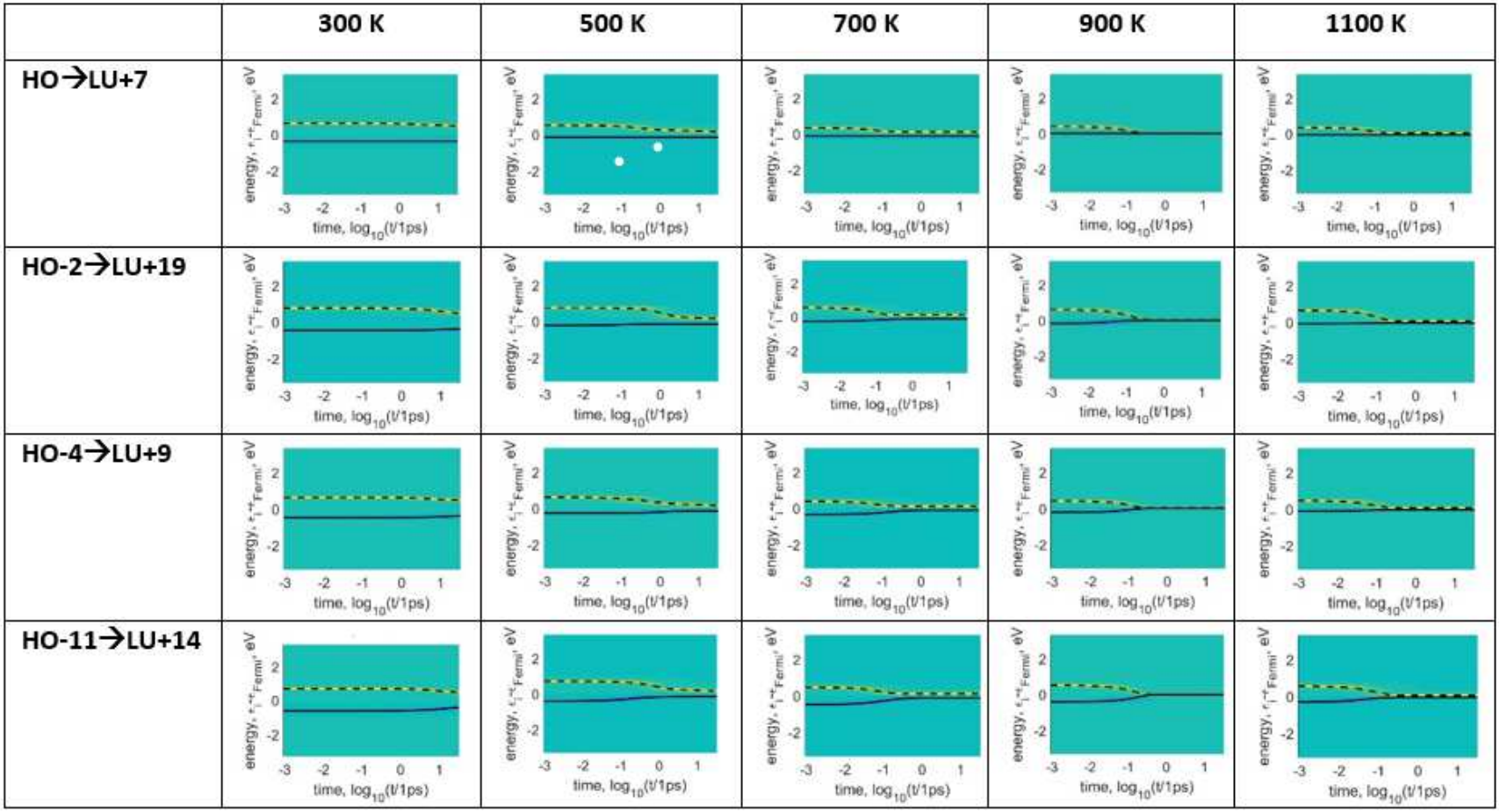

Figure 12. Dynamics of density distribution as function of energy. Yellow and Blue colors correspond to excess and deficiency of electron at certain energies at certain times. Green corresponds to equilibrium distribution. At lower temperatures, the change in energy for both the electron and hole are relatively negligible compared to higher temperatures. Note that one can consider relaxation rates for both electron and hole to be time derivatives of these graphs. Dashed line = electron expectation energy. Solid line = hole expectation energy

After computing the relaxation rates for both my electron & hole, several conclusions are apparant. First, in figure 12 density distribution as a function of energy by using density matrix dynamics (which studied how density changed with time). They are computed according to equation 14. Yelow and Blue colors corresponds to excess $n(\varepsilon, t) > 0$ and deficiency $n(\varepsilon, t) < 0$ of electron at certain energy, at certain time. Green corresponds to equilibrium distribution $n(\varepsilon, t) = 0$. The expectation values of electron and hole energy were computed by equations 15(a) and 15(b) and represented by dashed and solid line, respectively. Note that at lower temperatures the electron and hole relaxation rates were almost negligible. However, at higher values of temperatures relaxation occurs at earlier times. There is one expected trend from these figures. As the temperature increases, the energy difference between the electron and hole decreases. These findings agree with figure 8.

In figure 13, density distribution is studied in relation to the electron's position in space, computed with equation 19.. Two conclusions can be inferred from a qualitative examination of the graphs. First, all charge transfer is localized near the iodine dopants. This finding agrees with the chemical nature of iodine. Since iodine only needs one valence electron to complete its outer shell, it makes sense that an electron from the sodium dopant would travel toward the iodine dopant. Also, the electron appears to be traveling to the outermost iodine dopant.

Furthermore, the transition rate (fs^{-1}) increases with temperature until 700K after which it plateaus. That is, the higher the temperature the greater the electron's displacement between its initial and final points. This finding agrees with figure 6. At initial temperatures, only outlier orbital transitions away from the HOMO and LUMO had the greatest rates. However, as the temperature increases all orbital transitions, including the ones near HOMO and LUMO have nearly equal probability. The electron can travel greater distances because it has a greater number of pathways

available to it. Greater number of states implies more kinetic energy for the electron to travel greater distances.

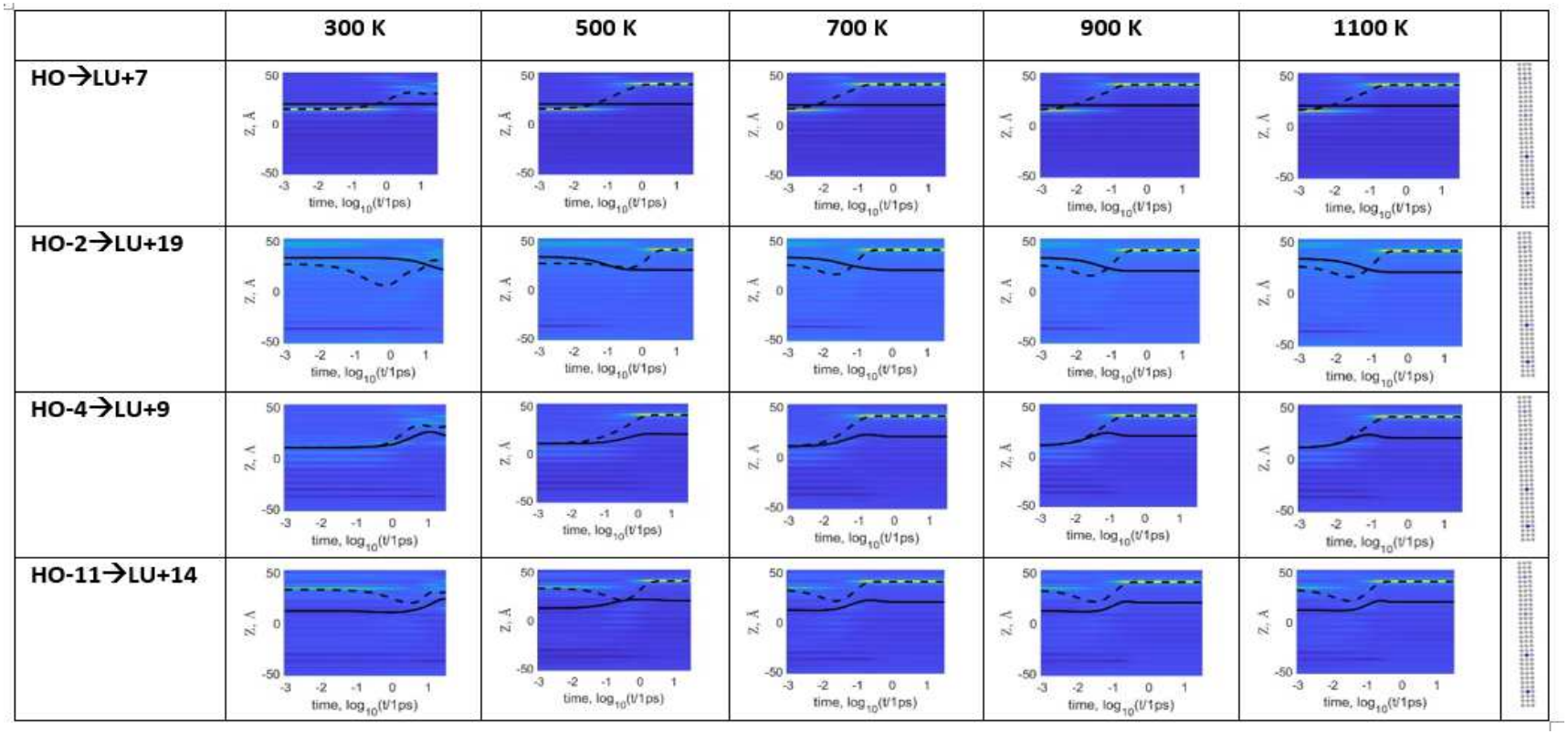

Figure 13**.** Dynamics of density distribution as function of distance. Solid line = hole energy; Dashed line = electron energy. Yellow = excess of electron. Green = excess of hole. Blue = equilibrium. Note that all charge transfer is localized around the iodine dopants and that the transition rates increase with temperature.

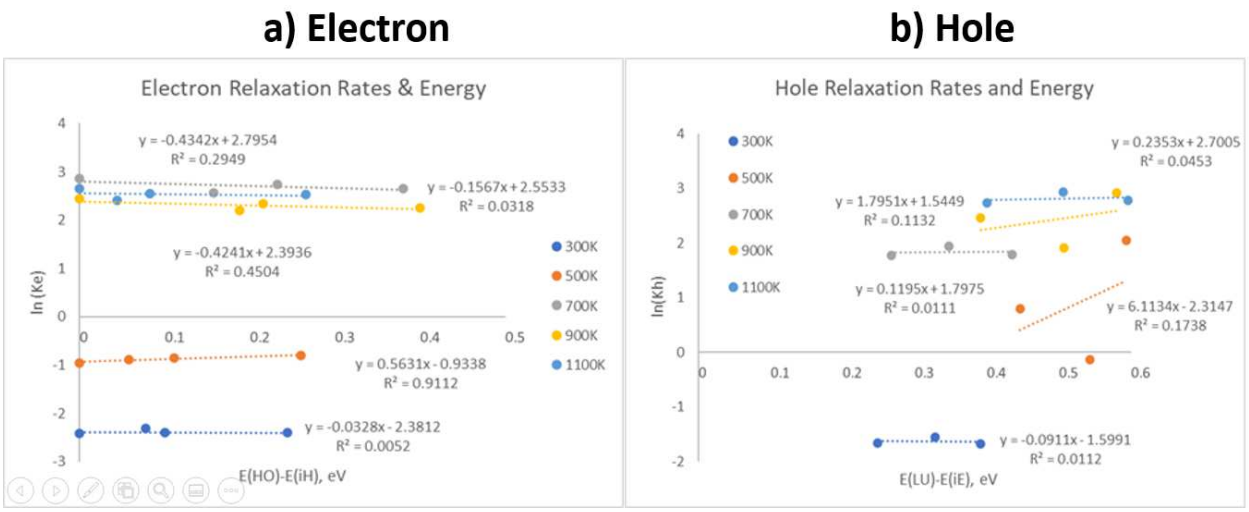

Figure 14. Relaxation rates as a function of energy. Relaxation rates for both the electron and hole were fitted to the bandgap law to quantitively determine their correlation. Results demonstrates moderate correlation for electron and little correlation for the hole.

Figure 14 reports rates computed by equation 17 for different initial excitations of the model and at different temperatures. In figure 14, a more quantitative examination is taken. Relaxation rates are studied as a function of energy. A look at 11(a) shows that the bandgap law ($K_{e/h} = Ae^{-\alpha \Delta E}$) appears to only apply to orbital transitions at higher temperatures. Also, there is negligible change of the relaxation rate with energy at the lower temperatures. Perhaps one reason for this is due to the decrease with the bandgap with respect to temperature as figure 5 demonstrates. When the bandgap decreases at higher temperatures (this is corroborated by figure 9), the 'energy' an electron needs to emit decreases. As a result, it is easier for an electron to go down an orbital. 11(b) shows limited correlation of the hole with the bandgap law.

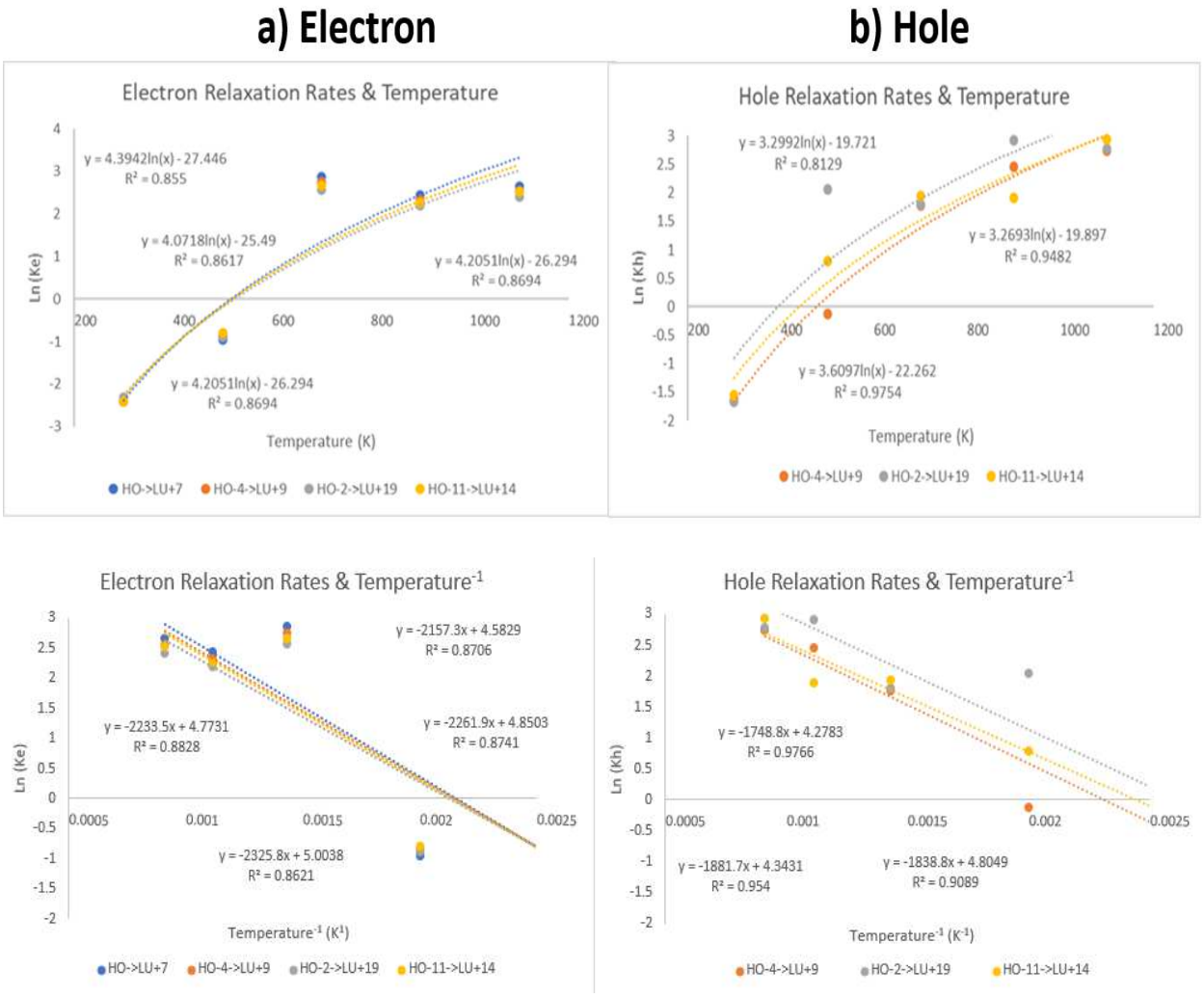

Figure 15. Relaxation rates as a function of temperature and temperature^{-1}. Results show that the change of relaxation rates with respect to temperature is very similar regardless of initial orbital conditions. This demonstrates that the relaxation rates follow a Boltzmann distribution.

Additionally, figure 15 shows that the dependence of my electron and hole relaxation rates with temperature are independent of orbital transitions. In simpler term, all orbital transitions return to their original state at the same rate no matter what temperature is examined. A qualitative examination of these figures illustrates that these figures are Boltzmann distributions, where the relaxation rates have an exponential relation to temperature. Specifically, this proves that $\alpha = 1/k_B T$ where T is temperature and k_B is the Boltzmann constant.

DISCUSSION

The major purpose of this study is to determine the degree to which electron and hole relaxation rate follows the bandgap law. If they follow the bandgap law, then experimentalists can save time and just compute relaxation rates. There is no need for experiments to compute the rates. Fortunately, figure 11 shows that electrons follow the bandgap law at higher temperatures and not at lower temperatures. This is adequate. In the modern world semiconductors are used in every appliance and accessory. Since they operate at the high temperatures examined in this study, the bandgap law is very applicable for charge transfer in these situations. Unfortunately, there is little correlation in my study between hole relaxation rates and the bandgap law. Note that further computational studies must be done to corroborate these findings.

Figures 10 & 11 show how the orbitals are localized on their respective dopants. As noted, in this case the occupied and occupied orbitals are localized on the sodium and iodine dopants, respectively. However, this only applies when examining individual orbital transitions. However, oftentimes scenarios where an electron transitions between superpositions of orbitals appear. This is only the simplest case. This superposition scenario often occurs in real-world applications such as semiconductors in appliances. Future studies of charge transfer of doped lead telluride nanowires should look at this more difficult scenario for improved analysis of real-world applications.

Figures 9 & 8 examine how the orbital energies change with temperature. As noted in the results section, as the temperature increases, the bandgap decreases. However, two causes are in play here. One cause is obviously the change to higher temperatures. In contrast, there is also a dependence on time. In these simulations and figures the time for heating and molecular dynamics is very short. However, if we extend the simulation time, we will likely see a smaller change in

the bandgap, especially at the higher temperatures. In other words, we will likely see that at 700K, 900K, and 1100K, that the bandgap has very little change.

Figures 7 & 6 give more information as to how the nanowire system changes with energy. In figure 4, note that less energy is absorbed for the doped nanowire than the undoped nanowire. This means that the transition rate for this system is higher than in the undoped original version. This accomplishes one of the original goals: strengthen the transition rates so that the rate of charge transfer increases. Thus, when applying this system to contemporary semiconductors, we will obtain an improved performance from our technology in modern life.

Figure 6 contrasts the density of states for a doped and undoped nanowire. It seems that the bandgap for the doped nanowire has slightly decreased. This shows that the nanowire's conductivity has slightly increased. Additionally, a qualitative examination of the two graphs shows that more states are available for the doped nanowire than the original model. This means that experimentalists have more control over the doped nanowire's electronic states and more options available to them than in the original counterpart.

CONCLUSIONS

In conclusion, this first principles numerical experiment has yielded many interesting findings. One such result is that doping improves a lead telluride nanowire's measure of charge transfer. Specifically, replacing two lead and two telluride atoms with sodium and iodine respectively substantially increases the measure of charge transfer. When contrasting results for a doped and undoped model, one finds that co-doped lead telluride has a lower rate of absorbing photoenergy at the bandgap. Note that it could still be efficient above the gap. This in turn leads to faster phonon-induced transitions between the conduction and valence bands.

The most important aspect of this study is how well the energy relaxation rates correlate with the bandgap law. There are two fashions of relaxation: subsequent and parallel. Only subsequent pathway of relaxation follows the gap law. The parallel pathway often violates gap law as there are more and more parallel channels available as one increases excitation energy. This atomistic computational study shows that in the studied material/nanostructures, the bandgap law only applies to electrons at higher temperatures and shows little correlation with the relaxation rates of holes. Furthermore, this study has shown that relaxation rates' dependence on temperature is independent of initial choice of photoexcited orbitals.

However, in the future, researchers in the area of computational materials science could be interested in analyzing transitions starting from initial conditions represented by a superposition of orbitals to determine if the bandgap law still applies in that situation. This is important since many real-world applications have this type of initial photoexcitation. Also, computational chemists and physicists may wish to contrast the findings of this numerical experiment with exploration of other models, such as a doped and undoped helical model (figure 15) corresponding to a nanowire grown in <111> direction. Relaxation rates, density of states, absorption spectra and

other observables may need to be computed to compare with this study. Note that previous studies have shown that there is no momentum dispersion for helical nanowires. Furthermore, doping a helical nanowire is expected to affect its initial negligible bandgap.

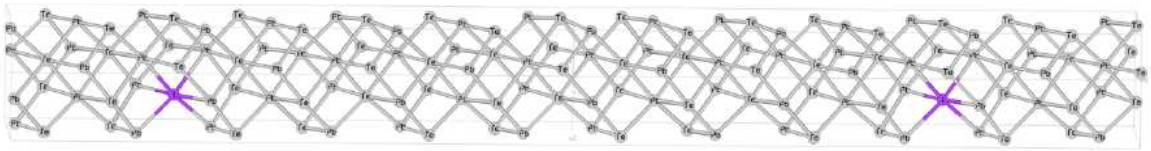

Figure 16[41]. Helical nanowire doped with Iodine. Future studies may examine charge transfer for this configuration or a co-doped model and subsequently compare with the results of this study.

The findings, observations, and trends obtained in this atomistic computational modeling of photoinduced dynamics in certain classes of nanostructures have a wide potential of applicability to industry. First, this work provides a numerical proof of intuitively expected trend that doping facilitates charge transfer. Second, for a long time, researchers and producers have needed to undergo long and laborious studies to calculate relaxation rates for a material. However, if future studies corroborate the findings of this work and prove that the bandgap law has at least limited applicability, then the time for research and development in industry can be greatly reduced. Additionally, the greater the correlation between the relaxation rates and the bandgap law, the more efficient a thermoelectric material is.

REFERENCES

1. Snyder, G.J. *Figure of merit ZT of a thermoelectric device defined from materials properties*. Energy and Environmental Science, 2017. **10** (11): 2280–2283.
2. Kong, Ling Bing. *Waste Energy Harvesting*. Lecture Notes in Energy, 2014. **24**. Springer. pp. 263–403.
3. Heremans, J. P.; Jovovic, V.; Toberer, E. S.; Saramat, A.; Kurosaki, K.; Charoenphakdee, A.; Yamanaka, S.; Snyder, G. J. *Enhancement of Thermoelectric Efficiency in PbTe by Distortion of the Electronic Density of States.* Science, 2008. **321** (5888): 554–7.
4. Pei, Yanzhong; Lalonde, Aaron; Iwanaga, Shiho; Snyder, G. Jeffrey. *High thermoelectric figure of merit in heavy hole dominated PbTe*. Energy & Environmental Science, 2011. **4** (6): 2085.
5. Pei, Yanzhong; Shi, Xiaoya; Lalonde, Aaron; Wang, Heng; Chen, Lidong; Snyder, G. Jeffrey. Convergence of electronic bands for high performance bulk thermoelectrics. Nature, 2011. **473** (7345): 66–9.
6. Quick, Darren. *World's most efficient thermoelectric material developed*. *Gizmag, 2012*.
7. Biswas, K.; He, J.; Blum, I. D.; Wu, C. I.; Hogan, T. P.; Seidman, D. N.; Dravid, V. P.; Kanatzidis, M. G. *High-performance bulk thermoelectrics with all-scale hierarchical architectures*. *Nature, 2018*. **489** (7416): 414–418.
8. Voudoukis, N. *Photovoltaic Technology and Innovative Solar Cells.* European Journal of Electrical Engineering and Computer Science, 2018. **2** (1).
9. Redfield, A.G., *On the theory of relaxation processes.* IBM Journal of Research and Development, 1957. **1**(1): p. 19-31.

10. Nitzan, A., *Chemical Dynamics in Condensed Phases : Relaxation, Transfer and Reactions in Condensed Molecular Systems*. 2006: OUP Oxford.

11. Webb, S.P., T. Iordanov, and S. Hammes-Schiffer. *Multiconfigurational nuclear-electronic orbital approach: Incorporation of nuclear quantum effects in electronic structure calculations.* Journal of Chemical Physics, 2002. **117**(9): p. 4106-4118.

12. Hammes-Schiffer, S. *Avoiding the Born-Oppenheimer separation between electrons and nuclei: Explicitly correlated wavefunctions and multicomponent density functional theory.* Abstracts of Papers of the American Chemical Society, 2011. **242**.

13. Tully, J.C., *Molecular-dynamics with electronic-transitions.* Journal of Chemical Physics, 1990. **93**(2): p. 1061-1071.

14. Kilina, S.V., et al. *Ab initio time-domain study of phonon-assisted relaxation of charge carriers in a PbSe quantum dot.* Journal of Physical Chemistry C, 2007. **111**(12): p. 4871-4878.

15. Kilina, S.V., D.S. Kilin, and O.V. Prezhdo. *Breaking the Phonon Bottleneck in PbSe and CdSe Quantum Dots: Time-Domain Density Functional Theory of Charge Carrier Relaxation.* Acs Nano, 2009. **3**(1): p. 93-99.

16. Kilina, S.V., et al. *Theoretical Study of Electron-Phonon Relaxation in PbSe and CdSe Quantum Dots: Evidence for Phonon Memory.* Journal of Physical Chemistry C, 2011. **115**(44): p. 21641-21651.

17. Fernandez-Alberti, S., et al. *Nonadiabatic Molecular Dynamics Simulations of the Energy Transfer between Building Blocks in a Phenylene Ethynylene Dendrimer. Journal of Physical Chemistry A, 2009.* **113**(26): p. 7535-7542.

18. Fernandez-Alberti, S., et al. *Unidirectional Energy Transfer in Conjugated Molecules: The Crucial Role of High-Frequency C C Bonds.* Journal of Physical Chemistry Letters, 2010. **1**(18): p. 2699-2704.

19. Nelson, T., et al. *Nonadiabatic Excited-State Molecular Dynamics Modeling of Photoinduced Dynamics in Conjugated Molecules.* Journal of Physical Chemistry B, 2011. **115**(18): p. 5402-5414.

20. Nelson, T., et al. *Nonadiabatic excited-state molecular dynamics: Numerical tests of convergence and parameters.* Journal of Chemical Physics, 2012. **136**(5).

21. Rego, L.G.C. and V.S. Batista. *Quantum dynamics simulations of interfacial electron transfer in sensitized TiO2 semiconductors.* Journal of the American Chemical Society, 2003. **125**(26): p. 7989-7997.

22. Craig, C.F., W.R. Duncan, and O.V. Prezhdo. *Trajectory surface hopping in the time-dependent Kohn-Sham approach for electron-nuclear dynamics.* Physical Review Letters, 2005. **95**(16).

23. Tempel, D.G. and A. Aspuru-Guzik. *Relaxation and dephasing in open quantum systems time-dependent density functional theory: Properties of exact functionals from an exactly-solvable model system.* Chemical Physics, 2011. **391**(1): p. 130-142.

24. Parkhill, J.A., D.G. Tempel, and A. Aspuru-Guzik. *Exciton coherence lifetimes from electronic structure.* Journal of Chemical Physics, 2012. **136**(10).

25. Egorova, D., et al. *Modeling of ultrafast electron-transfer processes: Validity of multilevel Redfield theory.* Journal of Chemical Physics, 2003. **119**(5): p. 2761-2773.

26. Pollard, W.T. and R.A. Friesner. *Solution of the redfield equation for the dissipative quantum dynamics of multilevel systems.* Journal of Chemical Physics, 1994. **100**(7): p. 5054-5065.

27. Pollard, W.T., A.K. Felts, and R.A. Friesner. *The Redfield equation in condensed-phase quantum dynamics.* Advances in Chemical Physics, Vol Xciii, 1996. **93**: p. 77-134.

28. Jean, J.M., R.A. Friesner, and G.R. Fleming. *Application of a multilevel redfield theory to electron-transfer in condensed phases.* Journal of Chemical Physics, 1992. **96**(8): p. 5827-5842.

29. Sundstrom, V., T. Pullerits, and R. van Grondelle. *Photosynthetic light-harvesting: Reconciling dynamics and structure of purple bacterial LH2 reveals function of photosynthetic unit.* Journal of Physical Chemistry B, 1999. **103**(13): p. 2327-2346.

30. Kuhn, O., V. May, and M. Schreiber. *Dissipative vibrational dynamics in a curve-crossing system.* Journal of Chemical Physics, 1994. **101**(12): p. 10404-10415.

31. Davis, W.B., et al. *Electron transfer rates in bridged molecular systems: A phenomenological approach to relaxation.* Journal of Physical Chemistry A, 1997. **101**(35): p. 6158-6164.

32. Apanasevich, P.A., et al. *Statistics of dephasing perturbations and relaxational processes in a high-power optic field - Application to free-induction decay.* Journal of the Optical Society of America B-Optical Physics, 1986. **3**(4): p. 587-594.

33. Kolesov, G. and Y. Dahnovsky. *Correlated electron dynamics in quantum-dot sensitized solar cell: Kadanoff-Baym versus Markovian approach.* Physical Review B, 2012. **85**(24): p. 241309.

34. Kilin, D.S. and D.A. Micha. *Relaxation of Photoexcited Electrons at a Nanostructured Si(111) Surface.* Journal of Physical Chemistry Letters, 2010. **1**(7): p. 1073-1077.

35. Chen, J., A. Schmitz, and D.S. Kilin, *Computational simulation of the p-n doped silicon quantum dot.* International Journal of Quantum Chemistry, 2012. **112**: p. 3879.

36. Hohenberg, P.; Kohn, W. *Inhomogeneous Electron Gas.* Physical Review 1964, **136** (3B), B864-B871.

37. Kresse, G.; Furthmüller, J. *Efficient iterative schemes for ab initio total-energy calculations using a plane-wave basis set.* Physical Review B 1996**, 54** (16), 11169-11186.

38. Kohn, W.; Sham, L. J. *Self-Consistent Equations Including Exchange and Correlation Effects.* Physical Review 1965**, 140** (4A), A1133-A1138.

39. Perdew, J. P.; Burke, K.; Ernzerhof, M. *Generalized Gradient Approximation Made Simple.* Physical Review Letters 1996**, 77** (18), 3865-3868.

40. Perdew, J. P.; Burke, K.; Ernzerhof, M. *Generalized Gradient Approximation Made Simple [Phys. Rev. Lett. 77, 3865 (1996)]*. Physical Review Letters 1997, 78 (7), 1396-1396.

41. Gima, Kevin. *Are PbTe nanowires ideal thermoelectric materials for semiconductors?* Dmitri Kilin 2019.